Tomographic Characterization of a Multi-Functional Composite High Impedance Surface

Kelvin J. Nicholson, *Member, IEEE,* Thomas C. Baum, *Member, IEEE*, Richard Ziolkowski, *Fellow, IEEE,* Kamran Ghorbani, *Senior Member, IEEE,* and Greg Bain

***Abstract*—The performance of a multi-functional composite high impedance surface (HIS) has been evaluated using the coherent Doppler tomography (CDT) and finite impulse response (FIR) filtering techniques. The HIS was fabricated using a combination of embroidery and advanced laser manufacturing processes. The result is a new conformable multi-functional glass fiber re-enforced polymer (GFRP) substrate suitable for structural load-bearing smart skin applications. The CDT method was utilized because it enabled the generation of a high resolution tomographic map of the HIS reflectivity. Tomograms generated at high incidence angles (> 80° from normal) were used to localize and FIR filter unwanted scattering associated with the ground plane edges and HIS transition regions. The resulting scattered fields from a defect (metallic block positioned in the center of the tomogram) were then used to assess the surface wave absorption within the HIS. Measured and simulated results are in excellent agreement.**

***Index Terms*—Artificial magnetic conductor, high impedance surface, high impedance ground plane, meta-absorber, multi-functional structures, pregtronics**

I. Introduction

CONFORMAL load-bearing smart skins (CLSS) are seen as a new avenue of research to enable multi-functional structural components [1]-[7]. These new multi-functional components exhibit optimized electrical and mechanical properties which may enhance the capability of an aerospace platform [2]. For example, conformal load-bearing antenna structures (CLAS) have been seen as one solution to CLSS where structural weight savings can be gained by integrating antennas in typical composite laminates. Examples of CLAS include the Slotted Waveguide Antenna Stiffened Structure (SWASS) concept [3], [7] and liquid metal vascular antennas [8]-[9], to name a few.

To enhance the utility of CLAS, it is desirable to incorporate artificial magnetic conductors (AMC) for manipulating ground plane surface currents [10], [11]. These structured ground planes may reduce electromagnetic coupling between adjacent antennas in an array configuration which is extremely desirable in applications where size restrictions exist, e.g., in unmanned aerial systems. In a similar regards, high impedance surfaces (HIS) have also been utilized to minimize or control surface wave propagation [11]. Since the band-gap response of a classical mushroom HIS is limited to approximately 30% ~ 40% [12], it is well suited to the comparatively narrow-band SWASS concept.

In the CLSS paradigm, it is advantageous to enable the manufacture of such metasurfaces in structural load-bearing composite laminates to reduce weight and minimize integration complexity. Experimental characterization of the classical mushroom HIS can be achieved using a variety of different propagation methods. The simplest is a specular reflection measurement. Other methods include transmission measurements using both probes and sources, parallel-plate waveguide measurements and free space transmission measurements [10]. However, it becomes extremely difficult to fully characterize the performance of a HIS which is physically large, adheres to a conformal structure or exhibits anisotropic properties. Moreover, probing the characteristics of such HIS can be extremely tedious and time consuming [13]. Furthermore, when using a propagation reflection method to obtain the reflected magnitude and phase [10] at low incidence angles (< 80° from normal), specular effects may dominate the results due to the finite nature of typical test specimens. In such cases the surface wave absorption properties of the HIS may be masked. Hence, these methods only give the cumulative response of the entire HIS test specimen.

This paper significantly expands previous work utilizing the coherent Doppler tomography (CDT) approach [14] to analyze HIS [15], [16]. The CDT method provides a more intuitive understanding of the scattering mechanisms occurring within the HIS through the use of a reflectivity map or tomogram. The finite impulse response (FIR) filtering of the scattered field enables the removal of unwanted features (such as the ground plane edges and HIS transition regions) that would otherwise mask the surface wave absorption characteristics of the HIS. Hence, the proposed combination of CDT and FIR

Manuscript received August 01, 2017. This work was supported by the Australian Department of Defense; Defense Science and Technology Group (DST Group) SRI-SME Program; the Defense Science Institute, an initiative of the State Government of Victoria; and the Australian Research Council grant number DP160102219.

G. Bain and K. J. Nicholson are with the Defense Science and Technology Group, Melbourne, Victoria 3207, Australia, (e-mail: greg.bain@dst.defence.gov.au; kelvin.nicholson@dst.defence.gov.au).

T. C. Baum and K. Ghorbani are with the School of Engineering, Royal Melbourne Institute of Technology, Melbourne, Victoria 3001, Australia, (e-mail: thomas.baum@rmit.edu.au; kamran.ghorbani@rmit.edu.au).

R. W. Ziolkowski is with the University of Technology Sydney, Global Big Data Technologies Centre, Ultimo NSW 2007, Australia, and the University of Arizona, Department of Electrical and Computer Engineering, 1230 E. Speedway Blvd., Tucson, AZ 85721, USA (e-mail: richard.ziolkowski@uts.edu.au).

techniques provide a significantly distinctive insight into the HIS scattering properties as compared to traditional methods [10].

This paper is structured as follows: Section II provides an overview of the composite HIS design. The HIS manufacturing process is outlined in Section III. Section IV introduces the CDT method and the simulation/measurement geometry. Section V demonstrates the FIR filtering method for feature extraction on simulated finite and infinite ground planes. Section VI outlines the experimental measurement setup. Section VII applies the CDT and FIR techniques to the measured scattering data from the fabricated HIS.

II. HIS Design

A classical mushroom-style HIS structure was designed to assess the utility of the CDT and FIR techniques for characterizing surface wave attenuation. Although there are many HIS designs which achieve optimal band-gap performance [12], the intent of this analysis is to evaluate the surface wave absorption properties in the presence of the proposed block and the finite ground plane geometry. Details of the HIS design and its manufacture are not the focus of this paper. Hence, this section will only briefly identify the key aspects of the HIS design. Section III will briefly describe the manufacturing process used to realize the HIS prototype employed in the measurement campaign. Further details of this manufacturing process can be found in [30].

Three cases will be examined to assess the efficacies of the proposed CDT and FIR techniques. The first case is based on the classical mushroom HIS. The second case is based on the HIS without vias (designated as an artificial impedance surface or AIS). The final case is based on the native dielectric substrate (with no vias or patches) to provide a comparative assessment.

The HIS was designed to exhibit a band-gap centered about 6.0 GHz. An illustration of the resulting HIS model (with dimensions) in the CST Microwave Studio 2017 simulation environment is given in Fig. 1. In the design of the HIS, two different simulations were performed. The first simulation focused on the specular performance (both magnitude and phase) of the HIS using Floquet ports with unit cell boundary conditions. The second simulation utilized the Eigen mode solver (with phase swept along the x axis) to determine the dispersion diagram of the HIS.

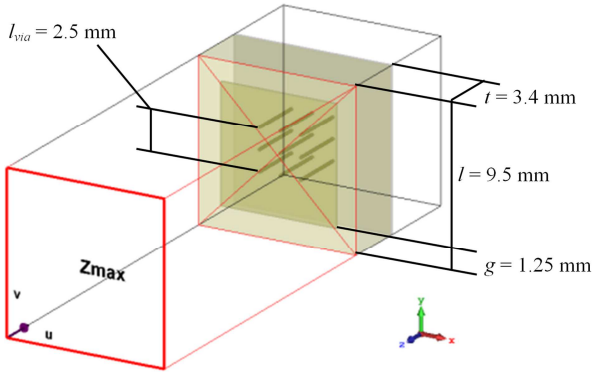

Fig. 1. CST unit cell model of the embroidered HIS mushroom structure.

The materials used to manufacture the substrate were 100 g/m^2 twill weave structural glass fabric (S-Glass) and Lonza PT-30 cyanate ester resin. The complex permittivity of the S-Glass / PT-30 composite substrate (once consolidated in an autoclave as per the Lonza recommended cure cycle) was measured to be ε_r = 4.046 + 0.0137i at 6.0 GHz using the Nicholson-Ross-Weir method [29] in a WR-137 waveguide. The patches were fabricated using nickel coated non-woven chopped-strand carbon fiber veil (Optiveil 20404E supplied by TFP) with a surface resistance of approximately 0.348 Ω/sq. The vias were fabricated using 100/34 dtex 2ply conductive thread (supplied by Shieldex) with a conductivity in the order of 3000 - 4000 S/m.

The benefit of using these materials over traditional off-the-shelf substrates (like FR-4) is that they provide an avenue to allow later fabrication of conformal load-bearing multi-functional composite HIS. These materials are fully compatible with existing aerospace composite tooling and manufacturing best practices. Therefore the HIS may potentially be prepared as a pre-preg for later use in a structural load-bearing smart skin application [30]-[32].

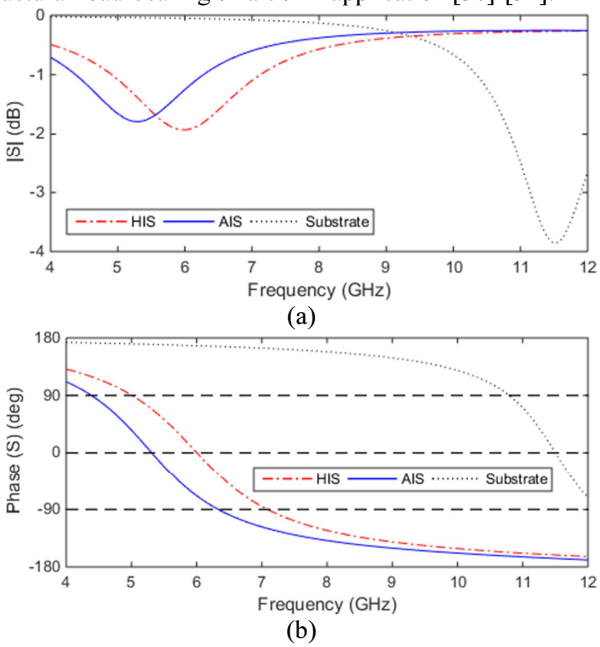

Fig. 2. Simulated (a) magnitude and (b) phase of the reflected field for the HIS, AIS and native substrate cases.

The simulated results are presented in Fig. 2. It can be seen that the HIS has a resonance at 6.0 GHz whereas the AIS structure has a resonance at 5.3 GHz and the native substrate has a resonance at 11.5 GHz. The ± 90° band-gap response of the HIS spans from 5.0 to 7.0 GHz giving a useful bandwidth of approximately 33%. The loss experienced in both the AIS and HIS structures (shown later in Section VII) is attributed to both the conductive losses (in the carbon veil and Shieldex thread) and the dielectric losses (in the S-Glass / PT-30 composite). It is worth noting that the native substrate (with a metallic ground plane) is acting like a traditional Salisbury screen, i.e., the resonance at 11.5 GHz is extremely close to $\lambda/4$ within the substrate material (t = 3.4 mm thickness with $\varepsilon_r \sim$ 4.0) at which the peak absorption occurs.

The dispersion diagram for all three cases is illustrated in Fig. 3. The dispersion diagram is more representative of the response of the structures under high incident angle illumination. According to the dispersion diagram, the HIS band-gap begins at 5.1 GHz (slightly higher than the specular performance in Fig. 2). Similarly, the AIS structure exhibits its first band-gap above 8.0 GHz while the native substrate experiences its first band gap above 11.0 GHz.

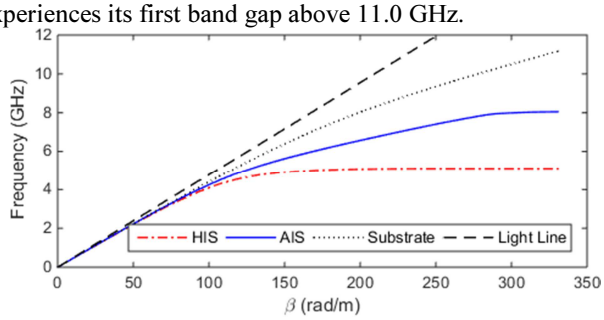

Fig. 3. Simulated dispersion diagram for the HIS, AIS and native substrate.

III. HIS Manufacture

The HIS was manufactured in a four-step process which differs for textile examples such as the HIS demonstrated in [33]. The first step was to embroider the via geometry into 25 plies of S-Glass fabric. The embroidery was done with a Brother PE-1000 embroidery machine. The completed HIS after the sewing process is shown in Fig. 4.

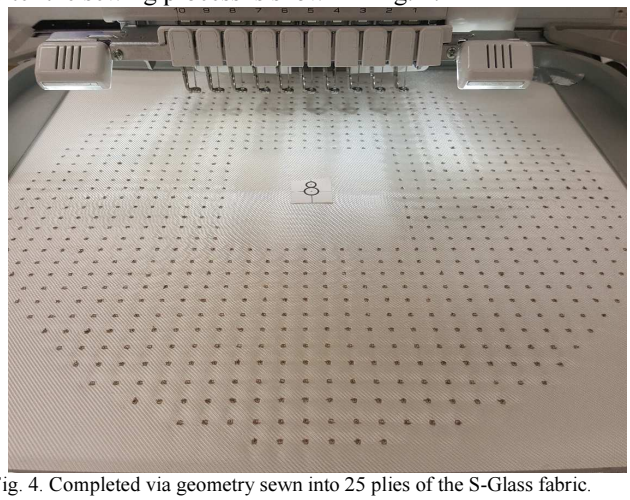

Fig. 4. Completed via geometry sewn into 25 plies of the S-Glass fabric.

The second step was to fabricate the ground plane from two plies of the carbon veil. The individual plies of the carbon veil were weakly adhered to the bottom face of the S-Glass laminate. The adhesive used was Selleys Kwik Grip contact adhesive.

The third step was to fabricate the patch geometry utilizing the carbon veil. This step was the most critical and the most complex to achieve. To begin, two plies of the carbon veil were weakly adhered to a single ply of the S-Glass fabric and de-bulked under vacuum for 30 minutes. A Trotec Speedy 400 80 W numerically controlled CO_2 laser was then used to profile the carbon veil to reveal the 'patch' geometry. The unwanted material (i.e., the veil between the patches) was peeled away and disposed. The single ply of the S-Glass (with carbon veil patches) was then aligned with the via geometry and infused with the Lonza PT-30 cyanate ester resin. The final HIS structure was cured at 200 ºC for 6 hours at 700 kPa pressure in an autoclave.

The final step consisted of machining the tapered edge (approximately 5.0°) and aperture for the 100.0 x 100.0 x 4.0 mm^3 aluminum block. The machining was completed on a MultiCAM numerically controlled router. The total diameter of the HIS was 390 mm. Due to the piece-wise approximation of a circle made by the patches, there is approximately 20 to 25 mm of tapered and flat dielectric before the outer ring of the HIS is reached. For interest, the fabricated HIS has a total equivalent density of approximately 2.4 g/cm^3. The conductive elements (i.e., the conductive thread and nickel coated carbon veil) contribute only a small fraction to the total weight of the HIS.

The AIS test article was manufactured in a similar fashion. However, the native substrate (manufactured from S-Glass / PT-30 with a carbon veil ground plane) was first fabricated and characterized to reduce the manufacturing effort. Two plies of the carbon veil were later bonded to the top face of the native substrate. The patch geometry was laser profiled directly on the consolidated substrate as illustrated in Fig. 5.

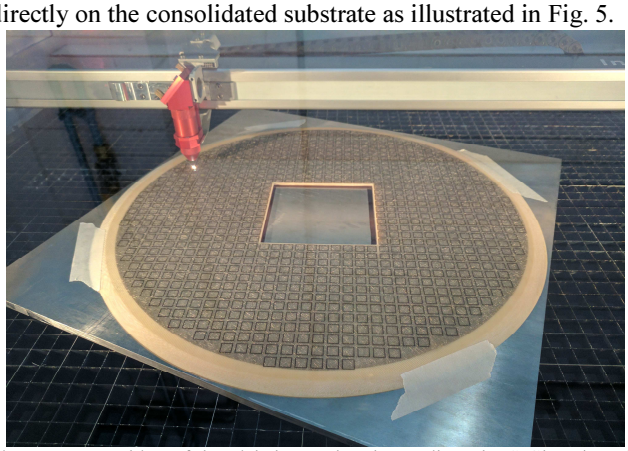

Fig. 5. Laser etching of the nickel coated carbon veil on the S-Glass / PT-30 substrate.

A quick check of the specular performance of each sample (HIS, AIS and substrate cases) was performed in a microwave anechoic chamber. Due to the large size of the structure, the specular return was measured in the near field. As such, the normalized specular response is presented relative to an aluminum reference target of the same dimensions.

Despite the measurement being performed in the near-field, a strong resonance about 6.0 GHz was observed for the HIS. This compares favorably with the CST simulations for normal incidence illumination. The extra loss seen above 6.0 GHz for the HIS is likely due to the resistive nature of the carbon veil material. The carbon veil is a non-woven mat and is extremely porous with potential for some anisotropy in the conductivity. This makes it extremely difficult to simulate. Consequently, a simplistic average bulk conductivity for the veil was used in the CST simulations. Similarly, no attempt was made to include the high permeability of the nickel coating in the CST simulation. Lastly, the manufactured AIS and substrate samples were thinner than expected (at approximately t = 3.0

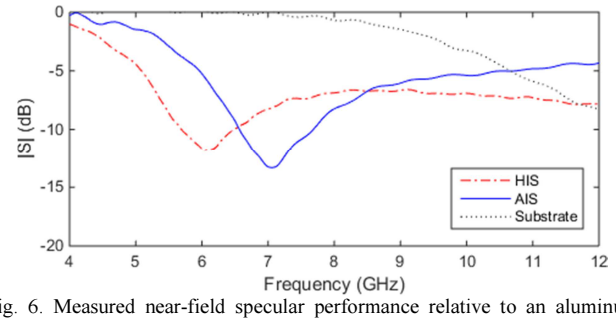

Fig. 6. Measured near-field specular performance relative to an aluminum reference target.

mm). Thus, the measured resonances occurred at higher frequencies as would be expected.

IV. CDT Technique

The reconstruction of a target from a set of scattering measurements is found in [17], [18]. However, the method introduced by Mensa ([19], [20]) and Hansen ([20], [21]) can achieve a higher degree of spatial resolution and is therefore well suited to microwave tomography.

Consider the measurement geometry illustrated in Fig. 7. This geometry differs slightly from the geometry presented in [19] – [21] as it includes the elevation angle (denoted here as α) of the transmit/receive antenna as measured from the image plane. In essence, it represents a quasi-spherical microwave tomography method [22]. This is important for the evaluation of surface waves which require high incidence angle

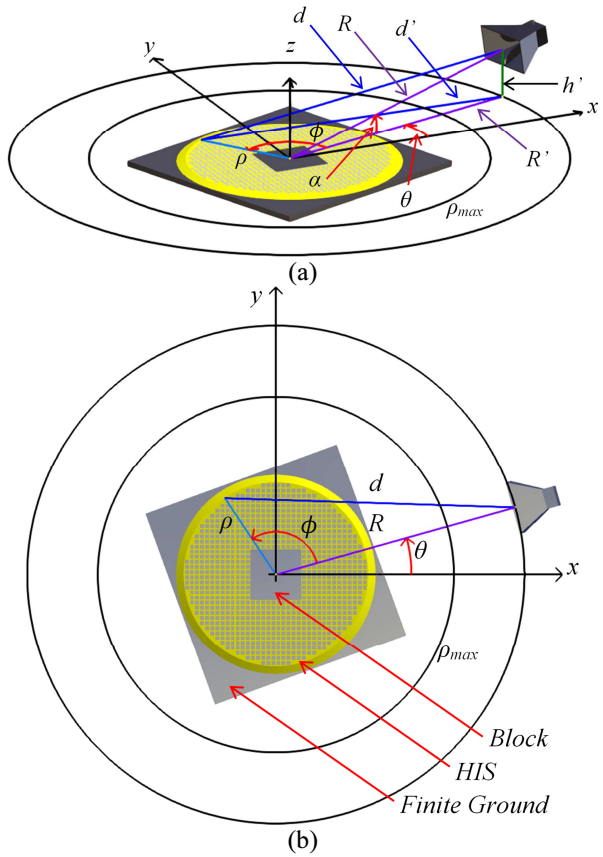

Fig. 7. (a) Perspective and (b) top view of the measurement geometry with finite ground, block and HIS.

illumination to be excited. The geometric parameters can be derived from their trigonometric relationships;

$$\begin{aligned} R' &= R\cos(\alpha) \\ h' &= R\sin(\alpha) \\ d' &= R'^2 + \rho^2 - 2\rho R'\cos(\phi) \\ d &= \sqrt{d'^2 + h'^2} \end{aligned} \tag{1}$$

where R is the radial distance between the antenna and the center of rotation, h' is the height of the antenna above the image plane, and d is the distance to each pixel in the image domain.

The tomographic approximation ($\hat{\psi}$) of the target reflectivity function (ψ) for a single illumination frequency is given by the equation;

$$\hat{\psi}(\rho,\phi|f) = \frac{4f}{c^2}\mathcal{F}^{-1}\left\{\mathcal{F}\{S(\theta|f)\}\cdot\mathcal{F}\left\{\frac{d}{R}e^{j\frac{4\pi f}{c}(d-R)}\right\}\right\} \tag{2}$$

where $S(\theta|f)$ is the scattering data measured at frequency f and illumination angle θ. Note that $\mathcal{F}\{\cdot\}$ and $\mathcal{F}^{-1}\{\cdot\}$ denote the forward and inverse Fourier transforms necessary to emulate a circular convolution over θ and ϕ. A composite image may then be generated by summation over a number of measured frequency points (N_f) according to the equation;

$$\hat{\psi}(\rho,\phi) = \Delta f\sum_{n=1}^{N_f}\hat{\psi}(\rho,\phi|f_n) \tag{3}$$

where Δf is the spectral sampling step. This composite image achieves a significant improvement in the dynamic range. However, the ability to resolve an image utilizing either a single frequency (2) or a bandwidth of frequencies (3) is invaluable for assessing typically narrow-band structures such as the HIS.

The maximum radius of the tomogram (denoted by ρ_{max} in Fig. 7 (a)) is governed by the angular sampling (denoted by $\Delta\theta$) and the maximum illumination frequency (denoted by f_N). A point in the tomogram at radius ρ_{max} must obey the Nyquist criteria;

$$\rho_{max}\sin(\Delta\theta) \le \frac{c_0}{2f_N} \tag{4}$$

where c_0 is the speed of light, to ensure that it does not exceed π radians between consecutive angular measurements. For example, with f_N = 18.0 GHz and $\Delta\theta$ = 0.5°, then $\rho_{max} \approx$ 0.9 m. However, to ensure an un-aliased tomogram, it is prudent to set ρ_{max} < 0.45 m (i.e. half the calculated value). The resolution of the tomogram can then be estimated from the first null in the point spread function. If the spectral bandwidth extends from 2.0 GHz to18.0 GHz, the tomogram resolution can be obtained by setting S = 1 for all frequencies and illumination angles. In this case the resolution of the tomogram is approximately 5.0 mm. This resolution is sufficient to localize and subsequently filter the small 100.0 × 100.0 × 4.0 mm^3 metallic block to be discussed in Section V.

To demonstrate the CDT technique, consider a finite ground plane illuminated by a TM polarized electromagnetic field. This field will induce a surface wave (often referred to as Sommerfeld-Zenneck surface wave [24]-[26]) that will propagate along the ground plane until it encounters an impedance mismatch (associated with a geometric or material

discontinuity) whereupon it will scatter and re-radiate. The angle of the main radiating lobe of this surface current can be estimated by the equation [27 p. 220];

$$\alpha \approx 49.35 \sqrt{\frac{c_0}{fL}} \tag{5}$$

where L is the characteristic length over which the surface wave at frequency f propagates. For example, consider a finite ground of dimension L = 400.0 mm illuminated by a TM field with frequency f = 18.0 GHz. The excited surface current will therefore radiate an angle $\alpha \approx 10°$. For lower illuminating frequencies, this lobe will move further away from the image plane resulting in a degradation of the tomogram sensitivity.

To further illustrate these concepts, a 400.0 x 400.0 x 7.0 mm^3 perfect electrically conducting (PEC) finite ground plane (off-set by 20° relative to the coordinate axes) with a 100.0 x 100.0 x 4.0 mm^3 PEC protruding block will be characterized. Note that this simulated target is illustrated in Fig. 7 along with the HIS. However, the HIS is not included in the following simulation. The tomographic reconstruction of this target for N_f = 81 uniformly spaced frequencies spanning a 2.0 to 18.0 GHz bandwidth and sampled at $\Delta\theta$ = 0.5° over a full 2π aperture is given in Fig. 8. The simulation was performed using the MLFMM method in the computational electromagnetic software package FEKO.

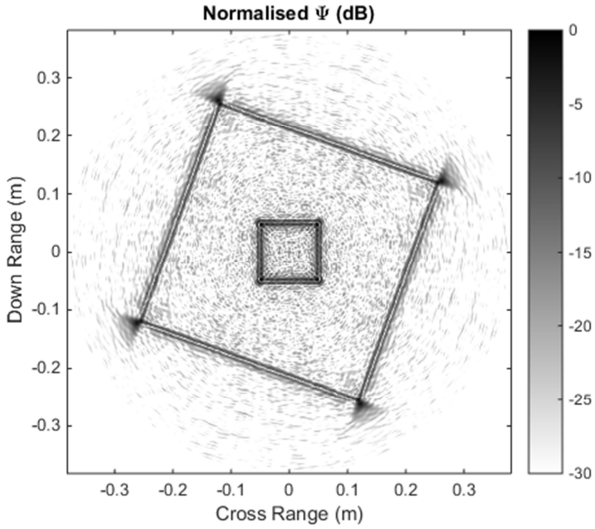

Fig. 8. Simulated tomographic reconstruction of the geometry in Fig. 7 (without HIS) using FEKO's MLFMM method.

The total radar cross section (RCS) of the geometry in Fig. 7 is presented in Fig. 9. The RCS of the target is presented at an altitude of α = 10° and an incidence direction of θ = 180° to ensure the result is not affected by Gibbs phenomena at the azimuth band edges. This is especially important in Section V where both the cross-range filtering (over the full 2π angular aperture) and the down-range filtering (over the 2.0 to 18.0 GHz bandwidth) will be applied.

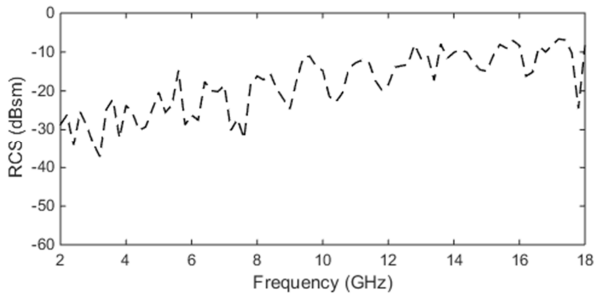

Fig. 9. Simulated RCS of the geometry associated with Fig. 8 from an altitude of α = 10° and an incidence direction of θ = 180°.

V. Feature Extraction

The scattering associated with a particular feature in the tomogram can be extracted by multiplication with a suitable two-dimensional band-pass gate in the spatial domain. Unfortunately, this approach to gating necessitates measurement of the spectral response over an infinite bandwidth. This requirement ensures that adjacent scatterers are well approximated by their respective delta functions in the spatial domain. However, since the measured data is fundamentally band limited, each scatterer exhibits a non-zero extent and, as a consequence, cannot be isolated in the spatial domain without erroneously incorporating a portion of its neighbor's spectrum.

The alternative approach is to convolve the spectral data (in the frequency domain) with the Fourier transform of the desired spatial gate [28]. The advantage of this approach is the finite nature of the spatial gate permits the analytical solution of its Fourier transform for all spectral frequencies. For example, a rectangular band-pass window has the well-known 'sinc' function as its Fourier transform.

The finite extent of the measured spectral content necessitates that the Fourier transform of the desired window be truncated to N_f samples when filtering in down-range or the number of theta angles (N_θ) when filtering in cross-range. This is analogous to multiplication by a second window function in the spectral domain. This second window can be selected to

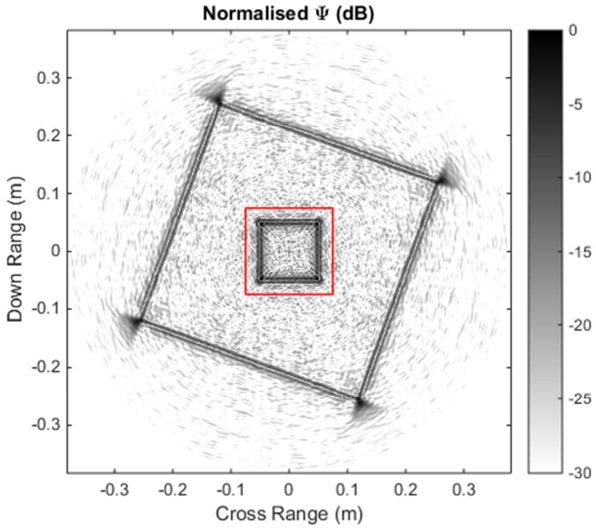

Fig. 10. FIR filter definition for the simulated geometry in Fig. 7.

minimize the Gibbs phenomenon associated with the bandwidth edges. Hence, this spectral filtering approach is the logical choice for use with the CDT technique where a sparse frequency sampling is sufficient to generate a high-resolution tomogram.

Consider the tomogram presented in Fig. 8. If the spectral content associated with the 100.0 x 100.0 x 4.0 mm^3 PEC block is of interest, then a rectangular gate (FIR filter) can be defined as illustrated in Fig. 10.

Convolving the spectral data with the Fourier transform of this rectangular gate yields the tomogram shown in Fig. 11. To be clear, the filtering operation was performed on the simulated spectral (*S*) data. The filtered spectral data was then processed as per Section IV to generate the tomogram in Fig. 11.

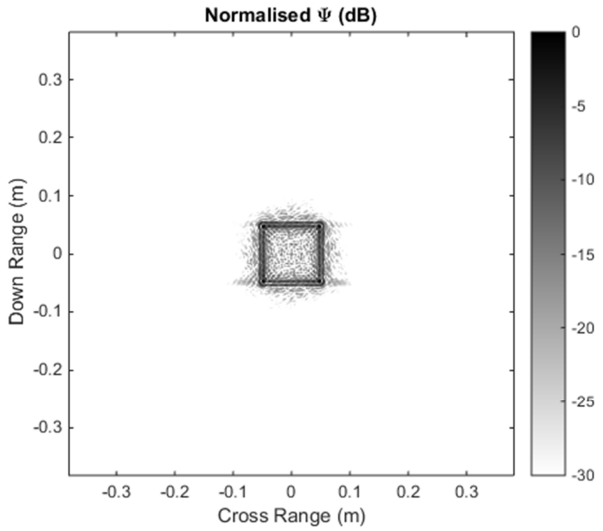

Fig. 11. Tomographic reconstruction of the FIR filtered geometry in Fig. 10.

It is difficult to distinguish which components of the RCS in Fig. 9 are associated with the PEC block or with the finite ground plane. However, after FIR filtering, the RCS of the PEC block (due to surface wave scattering from the geometric discontinuities at the block edges) can be determined in isolation from the finite ground plane. The result is presented in Fig. 12. For comparison, the RCS of the same PEC block on an infinite ground plane was determined in simulation to yield the second RCS given in Fig. 12. No FIR filtering of this spectral data is required as there are no features to remove that are associated with the infinite ground plane. Consequently, the simulated RCS is unaffected by Gibbs phenomena at the bandwidth edges.

The constructive / destructive RCS features illustrated in Fig. 12 are due to the excitation of a surface wave on the top face of the PEC block. This surface wave scatters from the leading and trailing edges of the PEC block resulting in the observed interference behavior.

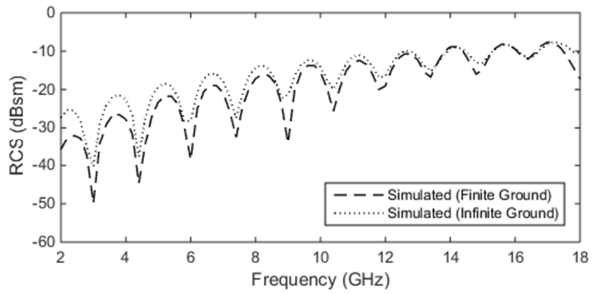

Fig. 12. Simulated RCS of the PEC block on a finite ground (after FIR filtering) and the same PEC block on an infinite ground plane from an elevation of $\alpha = 10°$ and incidence of $\theta = 180°$.

This RCS comparison in Fig. 12 clearly illustrates the utility of the CDT and FIR techniques. At the lower frequencies, the excited surface wave has not reached a steady state and so the total scattered field (after FIR filtering) is reduced relative to the infinite ground plane case. However, at the higher frequencies, the excited surface wave has reached steady state. Consequently, the finite ground plane result (after FIR filtering) agrees with the infinite ground plane simulation. Although it is not practical to measure an infinite ground plane, the 400.0 x 400.0 x 7.0 mm^3 finite aluminum ground provides a sufficient analog given the far-field criteria and the finite size of the anechoic chamber available for use by the authors.

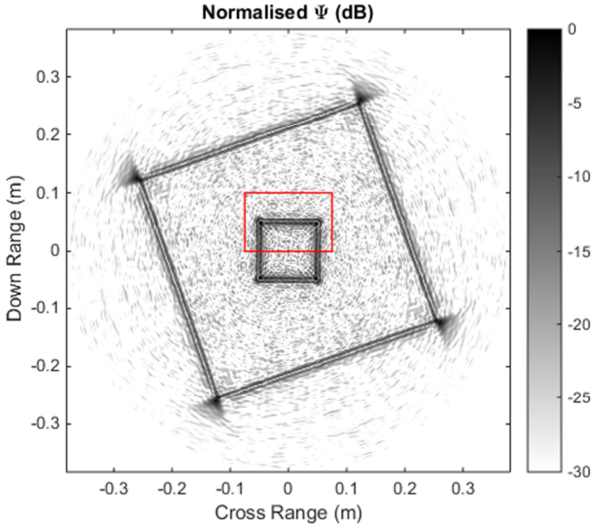

Fig. 13. FIR filtering to isolate the scattering associated with the leading edge of the PEC block.

For interest, it is possible to FIR filter just one of the PEC block edges as illustrated in Fig. 13. The spectral content associated with the region outlined in Fig. 13 can then be compared with the RCS of the FIR filtered PEC block. As is evident in Fig. 14, the interference pattern has been essentially removed. This is akin to a perfectly matched (to free space) trailing edge, which, albeit, is an impractical result. Nonetheless, this example demonstrates the deeper insight possible with the CDT and FIR techniques.

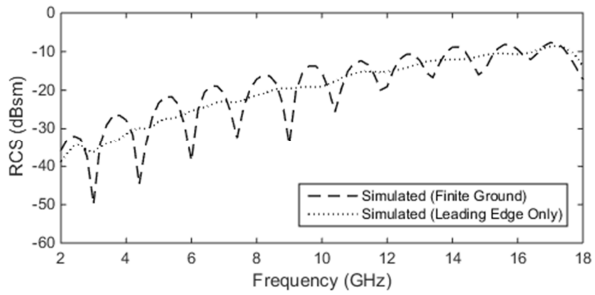

Fig. 14. Simulated RCS of the PEC block on a finite ground (after FIR filtering) compared with the leading edge scattering (after FIR filtering) for an elevation of $\alpha = 10°$ and incidence of $\theta = 180°$.

VI. Experimental Method

To evaluate the performance of the composite HIS structure, the CDT and FIR techniques were used. This necessitated the inclusion of the 100.0 x 100.0 x 4.0 mm^3 aluminum block embedded within the HIS structure to disrupt the excited surface wave. Comparison of the outcomes for the two cases (aluminum block with and without the HIS) on the finite ground plane are then used to illustrate the performance of the HIS.

Scattering measurements were performed in a microwave anechoic chamber using a calibrated Keysight N5225A PNA. The calibration process normalized the measured scattering parameters to a known target. In this case, it was a simple 150.0 x 150.0 mm^2 aluminum plate measured specularly from a distance of R = 5.0 m to ensure far-field illumination. The calibration procedure can be expressed as;

$$S_{cal}(\theta|f) = \frac{S_{measured}(\theta|f) - S_{iso}(\theta|f)}{S_{ref}(\theta|f) - S_{iso}(\theta|f)} \quad (6)$$

where S_{cal} is the calibrated scattering data, S_{ref} is the 150.0 x 150.0 mm^2 square aluminum calibration target and S_{iso} is the isolated chamber measurement.

Due to the large number of measurements necessary to achieve a full 2π aperture in $\Delta\theta$ = 0.5° steps, S_{iso} was influenced by phase noise as a result of temperature fluctuations within the PNA, coaxial cables, antennas and anechoic chamber. To minimize these error sources, S_{iso} was calculated by taking the average of $S_{measured}$ as;

$$S_{iso}(f|\theta) = \frac{1}{N_\theta}\sum_{n=1}^{N_\theta} S_{measured}(f|\theta_n) \quad (7)$$

where N_θ = 720 is the number of angular steps used to form the 2π aperture. This approach removed all zero Doppler components from the tomogram. Hence, any feature of interest in the tomogram that resides at the rotation center will be subtracted inadvertently. Therefore, as illustrated in Fig. 15, the finite aluminum ground plane and block were positioned on the Azimuth-over-Altitude mount in the anechoic chamber to avoid such issues.

Fig. 15. Measurement setup with only the finite ground plane and the block.

The HIS was placed around the 100.0 x 100.0 x 4.0 mm^3 aluminum block as illustrated in Fig. 16. Care was taken to ensure good electrical contact between the HIS and the finite aluminum ground plane. Unlike the simulated results in Section IV where computational resources and time limited the number of frequency samples used to generate the tomogram, the scattering data was measured with N_f = 401 samples over the entire 2.0 to 18.0 GHz bandwidth. This increased spectral sampling significantly improved the dynamic range of the tomogram as per equation (3).

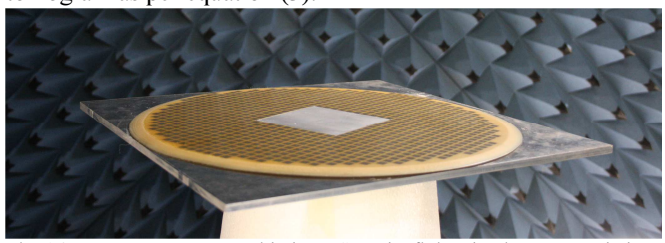

Fig. 16. Measurement setup with the HIS on the finite aluminum ground plane and with the aluminum block.

VII. Surface Wave Scattering

The measured tomogram and RCS (after FIR filtering) for the finite ground plane and block (shown in Fig. 15) are presented in Fig. 17 for later comparisons with the corresponding results obtained from the HIS, AIS and substrate cases.

The HIS was then installed as shown in Fig. 16. The measured tomogram and RCS (after FIR filtering) are presented in Fig. 18. The reconstructed tomogram illustrated in Fig. 18 (a) reveals the complex scattering that occurs within the HIS as a result of the via and patch geometry. There are three main features that can be identified in this tomogram.

The first identifiable feature is the transition between the finite ground plane and the tapered / flat substrate regions. This transition is illustrated by the thin light gray band that runs circumferentially around the HIS with an approximate width of 20 ~ 30 mm. In this region the surface waves are disrupted as they transition from free-space into the dispersive dielectric substrate.

The second feature is outlined by the darker region around the periphery of the HIS. This region is approximately 50 mm wide (about one wavelength at 6.5 GHz). In this region the surface waves are transitioning into the HIS structure.

The third region (closest to the aluminum block) is identified by a periodic speckle pattern (correlated with the corners of the HIS patches). In this region the surface wave has achieved a quasi-steady state. It must be noted that the tomogram represents the coherent summation of all scattering

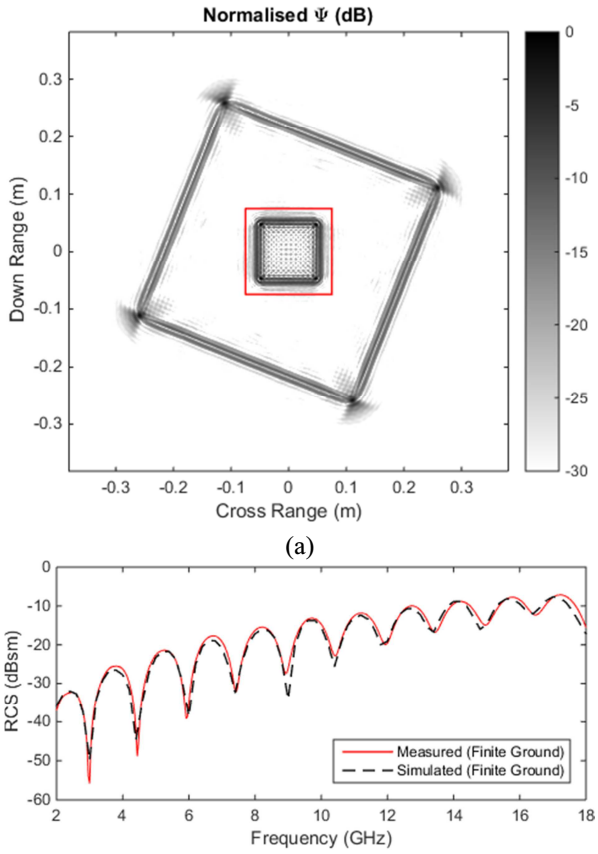

Fig. 17. Measured (a) tomogram and (b) FIR filtered RCS values of the block with no HIS from an elevation of $\alpha = 10°$ and incidence of $\theta = 180°$.

events over the 2.0 to 18.0 GHz bandwidth. Therefore, these scattering features (due to the physical sizes of their scattering centers) are mostly the result of the higher illumination frequencies.

As is evident in Fig. 18 (b), the HIS band gap is clearly present from approximately 5.0 GHz with a strong resonance at about 6.5 GHz. This is in reasonable correlation with the predicted band-gap results from the CST unit cell simulation given in Fig. 3. Hence, the surface wave scattering from the aluminum block has been significantly reduced as a result of the presence of the HIS. Fig. 18 (c) illustrates the effective isotropic performance of the HIS for all illumination angles at 6.5 GHz.

In Fig. 18 (b), the surface wave is seen to be strongly attenuated over a much larger bandwidth (extending up to approximately 14.0 GHz) then was predicted. To understand this extended performance of the HIS, the AIS sample (with no embroidered vias) was measured. Only the nickel coated carbon 'patches' were present on the PT-30 / S-glass substrate. The resulting measured tomogram and RCS values are presented in Fig. 19.

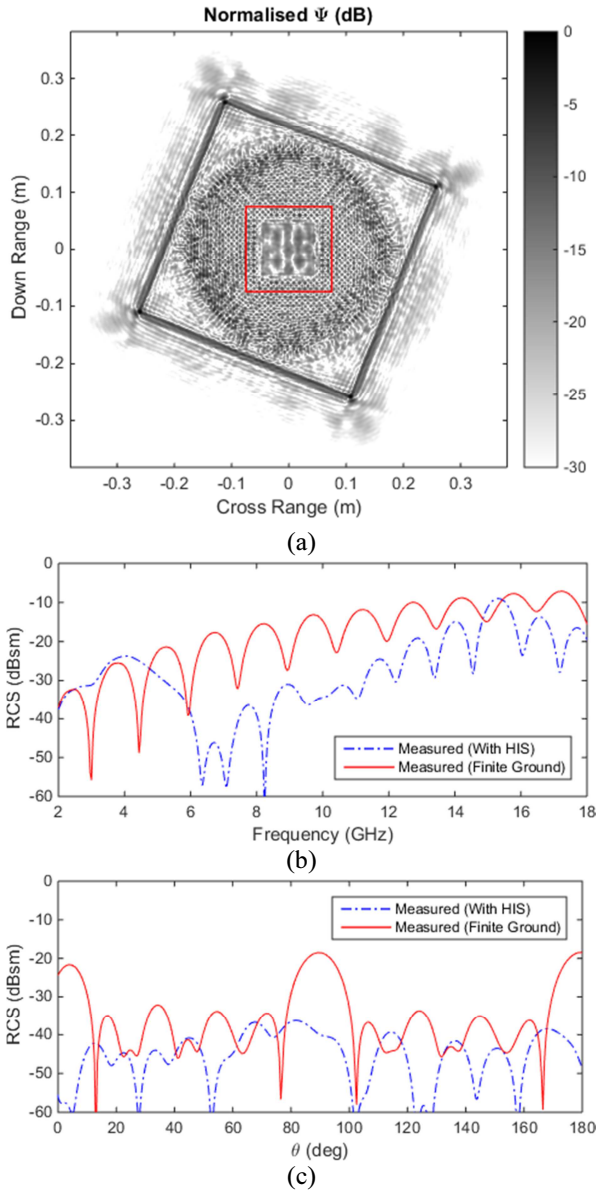

Fig. 18. Measured (a) tomogram and FIR filtered RCS values of the block with the HIS present from an elevation of α = 10° and (b) incidence of θ = 180° and (c) at 6.5 GHz.

Comparison of Fig. 18 (b) and Fig. 19 (b) confirms the strong resonance (about 6.5 GHz) present in the HIS results is due to the inclusion of the vias. The extended performance of the HIS can therefore be attributed to the resistive component of the nickel coated carbon veil patches and dielectric loss in the substrate.

For completeness, the native substrate sample was also measured and analyzed. The resulting tomogram and RCS (after FIR filtering) are presented in Fig. 20. As evident in Fig. 20 (b), the scattering reduction at the high frequencies (above 14.0 GHz) can be attributed solely to the dielectric loss in the substrate.

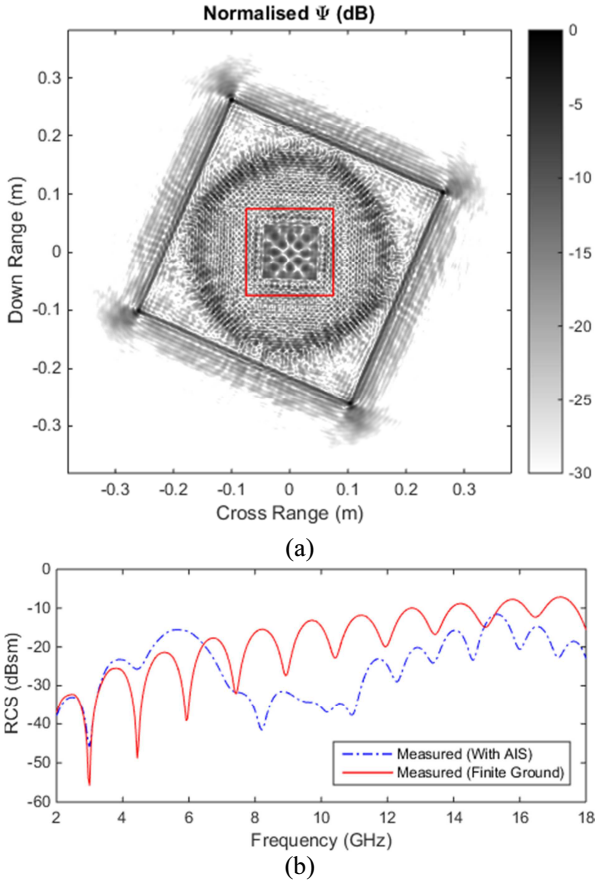

Fig. 19. Measured (a) tomogram and (b) FIR filtered RCS values of the block with the AIS (no vias) from an elevation of $\alpha = 10°$ and incidence of $\theta = 180°$.

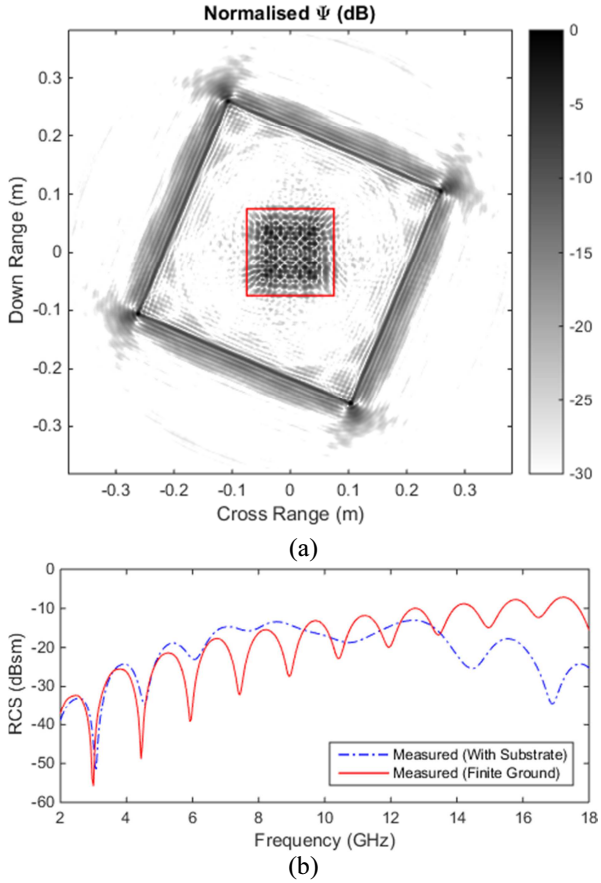

Fig. 20. Measured (a) tomogram and (b) FIR filtered RCS values of the block with the dielectric substrate (no vias or patches) from an elevation of $\alpha = 10°$ and incidence of $\theta = 180°$.

In summary, the CDT and FIR techniques have been employed to fully explain the scattering mechanisms present in the fabricated HIS structure. The measured surface wave absorption (determined using the CDT and FIR techniques) is in reasonable agreement with the simulated dispersion diagram in Fig. 3. The HIS clearly provides a significant improvement in the attenuation of the surface waves. Lastly, it should be noted that the large computational size of the HIS (due mostly to the inclusion of the electrically thin lossy conductors and dielectric materials) inhibits the numerical simulation of these structures in FEKO or CST (at least to within the computing power available to the authors). This further highlights the usefulness of the CDT and FIR techniques for the investigation of the scattering properties of electrically large HIS.

VIII. Conclusion

This work has demonstrated the application of the coherent Doppler tomography (CDT) and finite impulse response (FIR) filtering techniques to the characterization of the scattering from a simple mushroom-style HIS. The manufacturing techniques used to fabricate the HIS offer a unique approach for realizing multi-functional composite smart skins. The materials used are semi-structural, electrically thin, light weight and can potentially be prepared as a pre-preg for inclusion in a traditional composite laminate.

All three measured cases (HIS, AIS and substrate only) demonstrated good agreement with numerical simulation. The measured tomograms provide a unique insight into the scattering mechanisms of the composite HIS at high incidence angles over a wide bandwidth. The tomograms were used to identify the different scattering phenomena occurring within the HIS at the transitions between the finite ground plane and the substrate, into the HIS, and from the patches themselves. The FIR process was then used to filter out these transition regions to yield a true representation of the HIS performance (for an illumination angle of $\alpha = 10°$). The analysis demonstrated that the HIS not only forbids surface wave propagation over the band-gap region but (due to the high losses from the constituent materials) exhibits significant absorption up to 14.0 GHz. This information gained about the HIS from the CDT and FIR techniques has not been demonstrated previously in the literature to the best of the author's knowledge. The CDT and FIR techniques therefore provide a unique approach to characterizing electrically large HIS and AIS structures.

Acknowledgment

This work was supported by the Australian Department of Defence - Defence Science and Technology Group (DSTG) SRI-SME program and the Defense Science Institute (an

initiative of the State Government of Victoria and the Australian Research Council).

REFERENCES

[1] A. J. Lockyer, K. H. Alt, J. N. Kudva, R. W. Kinslow, and A. C. Goetz, "Conformal load-bearing antenna structures (CLAS): initiative for multiple military and commercial applications," in *Proc. SPIE3046, Smart Structures and Materials 1997*, San Diego, CA, Mar. 1997, pp. 182-196.

[2] M. Hopkins, J. Tuss, A. Lockyer, K. Alt, R. Kinslow, and J. Kudva, "Smart skin conformal load-bearing antenna and other smart structures developments," in *Proc. 38th Structures, Structural Dynamics, and Materials Conference*, American Institute of Aeronautics and Astronautics, Kissimmee, FL, Apr. 1997, pp. 521-530.

[3] P. J. Callus, "Novel concepts for conformal load-bearing antenna structure," Defence Science and Technology Organisation (DSTO), DSTO-TR-2096, 2008, pp. 1 - 111.

[4] H. S. Kim, J. S. Kang, J. S. Park, H. T. Hahn, H. C. Jung, and J. W. Joung, "Inkjet printed electronics for multifunctional composite structure," *Compos. Sci. Technol.*, vol. 69, issue 7-8. pp. 1256-1264, Jun. 2009.

[5] D. Gray, K. J. Nicholson, K. Ghorbani, and P. J. Callus, "Carbon fibre reinforced plastic slotted waveguide antenna," in *Proc. Asia-Pacific Microwave Conference*, APMC, Yokohama, Japan, Dec. 2010, pp. 307-310.

[6] A. V. Kumar, "Multifunctional Composite Structures," DTIC Document AFRL-RW-EG-TR-2010-047, 2010, pp. 1-128.

[7] K. J. Nicholson, W. S. T. Rowe, K. Ghorbani, and P. J. Callus, "Split-ring resonator loaded miniaturized slot for the slotted waveguide antenna stiffened structure," in *Proc. The Fifth International Congress on Advanced Electromagnetic Materials in Microwaves and Optics*, Metamaterials, Barcelona, Spain, Oct. 2011, pp. 540-542.

[8] D. J. Hartl, G. J. Frank, G. H. Huff, and J. W. Baur, "A liquid metal-based structurally embedded vascular antenna: I. Concept and multiphysical modeling," *Smart Mater. Struct.,* vol. 26, p. 025001, 2017.

[9] D. J. Hartl, G. J. Frank, R. J. Malak, and J. W. Baur, "A liquid metal-based structurally embedded vascular antenna: II. Multiobjective and parameterized design exploration," *Smart Mater. Struct.,* vol. 26, no. 2, 025002, 2017.

[10] D. Sievenpiper, "High-Impedance Electromagnetic Surfaces," Ph. D. dissertation, EE Dept., UCLA, Los Angeles, CA, 1999.

[11] D. Sievenpiper, Z. Lijun, R. F. J. Broas, N. G. Alexopolous, and E. Yablonovitch, "High-impedance electromagnetic surfaces with a forbidden frequency band," *IEEE Microw. Theory Techn.,* vol. 47, no. 11, pp. 2059-2074, Nov. 1999.

[12] C. R. Simovski, A. A. Sochava, and S. A. Tretyakov, "New compact and wide-band high-impedance surface," in *Proc. 2004 IEEE International Symposium on Antennas and Propagation*, Monterey, CA, June 2004, vol. 1, pp. 297-300.

[13] B. J. Justice, J. J. Mock, L. Guo, A. Degiron, D. Schurig and D. R. Smith, "Spatial mapping of the internal and external electromagnetic fields of negative index metamaterials," *Opt. Express*, vol. 14, no. 19, pp. 8694-8705, Sep. 2006.

[14] K. J. Nicholson and C. H. Wang, "Improved Near-Field Radar Cross-Section Measurement Technique," *IEEE Antennas Wireless Propag. Lett.,* vol. 8, pp. 1103-1106, Sep. 2009.

[15] K. J. Nicholson, T. Baum, K. Ghorbani, and R. W. Ziolkowski, "Microwave Doppler tomography of high impedance ground planes for aerospace applications," in *Proc. 2016 International Workshop on Antenna Technology (iWAT 2016)*, Cocoa Beach, FL, Mar. 2016, pp. 33-36.

[16] T. C. Baum, K. Ghorbani, and K. J. Nicholson, "Doppler tomographic investigations of a lossy high impedance surface absorber at high incident angles," in *Proc. 46th European Microwave Conference (EuMC 2016)*, London, UK, Oct. 2016, pp. 600-603.

[17] R. M. Mersereau and A. V. Oppenheim, "Digital reconstruction of multidimensional signals from their projections," *Proc. IEEE,* vol. 62, no. 10, pp. 1319-1338, Oct. 1974.

[18] R. M. Mersereau, "Direct Fourier transform techniques in 3-D image reconstruction," *Comput. Biol. Med.,* vol. 6, no. 4, pp. 247-258, Oct. 1976.

[19] D. Mensa, G. Heidbreder, and G. Wade, "Aperture synthesis by object rotation in coherent imaging," *IEEE Trans. Nucl. Sci.,* vol. NS-27, no. 2, pp. 989-998, Apr. 1980.

[20] D. L. Mensa, S. Halevy, and G. Wade, "Coherent Doppler tomography for microwave imaging," *Proc. IEEE,* vol. 71, no. 2, pp. 254-261, Feb. 1983.

[21] E. W. Hansen, "Circular harmonic image reconstruction: experiments," *Appl. Opt.,* vol. 20, no. 13, pp. 2266-2274, Jul. 1981.

[22] E. W. Hansen, "Theory of circular harmonic image reconstruction," *J. Opt. Soc. A,* vol. 71, no. 3, pp. 304-308, Mar. 1981.

[23] S. J. Norton and M. Linzer, "Ultrasonic reflectivity imaging in three dimensions: exact inverse scattering solutions for plane, cylindrical, and spherical apertures," *IEEE Trans. Biomed. Eng., vol. BME-28, no. 2,* pp. 202-220, Feb. 1981.

[24] J. H. Richmond, "Propagation of surface waves on an inhomogeneous plane layer," *IRE Trans. Microw. Theory Techn.,* vol. 10, no. 6, pp. 554-558, Nov. 1962.

[25] J. Wait, "A note on surface waves and ground waves," *IEEE Trans. Antennas Propag.,* vol. 13, no. 6, pp. 996-997, Nov. 1965.

[26] A. Ishimaru, J. D. Rockway, and L. Seong-Woo, "Sommerfeld and Zenneck wave propagation for a finitely conducting one-dimensional rough surface" *IEEE Trans. Antennas Propag.,* vol. 48, no. 9, pp. 1475-1484, Sep. 2000.

[27] E. F. Knott, J. F. Shaeffer, and M. T. Tuley, *Radar Cross Section*, 2nd edition. Raleigh, NC, SciTech Publishing, 2004.

[28] A. V. Oppenheim, *Discrete-time Signal Processing.* Pearson Education, India, 1999.

[29] W. B. Weir, "Automatic measurement of complex dielectric constant and permeability at microwave frequencies," *Proc. IEEE*, vol. 62, no. 1. pp. 33-36, Jan. 1974.

[30] T. C. Baum, R. W. Ziolkowski, K. Ghorbani, and K. J. Nicholson, "Embroidered active microwave composite preimpregnated electronics - Pregtronics," *IEEE Trans. Microw. Theory Tech.*, vol. 64, no. 9, pp. 3175-3186, Sep. 2016.

[31] K. Nicholson, O. Dunbabin, T. Baum and K. Ghorbani, "Characterisation of integrated microstrip lines in aerospace composite structure," Electron. Lett., vol. 53, no. 1, pp. 36-38, Jan. 2017.

[32] T. C. Baum, R. W. Ziolkowski, K. Ghorbani, and K. J. Nicholson, "Investigations of a Load-Bearing Composite Electrically Small Egyptian Axe Dipole Antenna," *IEEE Trans. Antennas Propag.,* vol. 65, no. 8, pp. 3827-3837, Aug. 2017.

[33] A. Tennant, W. Hurley, and T. Dias, "Knitted, textile, high impedance surface with integrated conducting vias," *Electron. Lett.,* vol. 49, no. 1, pp. 8-10, Jan. 2013.

Kelvin J. Nicholson (M'06) completed his B.Sc in Physics and B.Eng (Hons.) in Electrical Engineering from the University of Melbourne in 2005. He joined the Australian Department of Defence – Defence Science and Technology (DST) in 2006 as part of the Aerospace Composite Technologies group within the Aerospace Division. As part of this group, Kelvin has been involved in the development of microwave Doppler tomography imaging techniques for the assessment of damaged and repaired composite structures. He has assisted with the mitigation of electromagnetic interference issues aboard the ANZAC frigates and was awarded a Chief Defence Scientist Commendation in 2011 and a Royal Australian Navy Commendation in 2012. Kelvin completed his PhD in Electrical Engineering from RMIT University in 2014 with the support of the DST Enabling Research Program. His current research interests at DST include metamaterials and advanced composite materials for antenna and radar absorbing applications.

Thomas C. Baum (M'10) received his B.Eng in Aerospace Engineering (Hons.) at RMIT University in 2009. He completed his PhD. in electrical engineering for RMIT University in 2014. In 2015 he became a research fellow at RMIT University working on a variety of microwave related research areas including conformal load bearing antenna structures, coherent Doppler tomography and dielectric material characterization. His interests lie in novel antenna designs, radar systems, radar absorbing applications, scattering phenomena, microwave imaging, and material characterization.

Richard W. Ziolkowski (M'87–SM'91–F'94) received the B.Sc. (magna cum laude) degree (Hons.) in physics from Brown University, Providence, RI, USA, in 1974; the M.S. and Ph.D. degrees in physics from the University of Illinois at Urbana-Champaign, Urbana, IL, USA, in 1975 and 1980, respectively; and the Honorary Doctorate degree from the Technical University of Denmark, Kongens Lyngby, Denmark in 2012.

He is currently a Distinguished Professor with the Global Big Data Technologies Centre, University of Technology Sydney, Ultimo NSW, Australia. He is also a Litton Industries John M. Leonis Distinguished Professor with the Department of Electrical and Computer Engineering and a Professor with the College of Optical Sciences, The University of Arizona. He was the Computational Electronics and Electromagnetics Thrust Area Leader with the Lawrence Livermore National Laboratory, Engineering Research Division, before joining The University of Arizona, Tucson, AZ, USA, in 1990. He was the Australian DSTO Fulbright Distinguished Chair in Advanced Science and Technology from 2014-2015. He was a 2014 Thomas-Reuters Highly Cited Researcher. His current research interests include the application of new mathematical and numerical methods to linear and nonlinear problems dealing with the interaction of electromagnetic and acoustic waves with complex linear and nonlinear media, as well as metamaterials, metamaterial-inspired structures, and applications-specific configurations.

Prof. Ziolkowski is a Fellow of the OSA (Optical Society of America, 2006), and of the APS (American Physical Society, 2016). He served as the President of the IEEE Antennas and Propagation Society in 2005. He is also actively involved with the URSI, OSA and SPIE professional societies.

Kamran Ghorbani (M'96–SM'17) received the B.Eng (Hons.) and Ph.D. degree from RMIT University, Melbourne, VIC, Australia, in 1994 and 2001, respectively. From Nov. 1994 to 1996, he was a graduate RF Engineer with AWA Defence Industries working on early warning radar systems. In June 1996, he joined RMIT University to pursue his Ph.D. studies. From Dec. 1999 to March 2001, he was a Senior RF Engineer with Tele-IP working on VHF transceivers for commercial aircraft. He joined the Department of Communication and Electronic Engineering (now the School of Electrical and Computer Engineering) at RMIT University in 2001 as a continuing Academic.

Prof. Ghorbani is currently the Director of the Communication Technologies Research Centre, RMIT University. He is responsible for strategic planning and managing the research center. His research interests include, dielectric measurements, composite material structures, frequency selective surfaces, metamaterials, RF energy harvesting, radar systems, ferroelectric devices and multifunctional antennas.

Prof. Ghorbani was the Chair of Asia Pacific Microwave Conference APMC2011, which was held in Melbourne, Australia. He was the Co-Chair of Technical Program Committee for IEEE International Microwave and RF Conference, IMaRC2014, which was held in India. He was the Chair of first Australian Microwave Symposium, AMS2014, which was held in Melbourne, Australian. He is the Chair of Technical Program Committee of the Asia Pacific Microwave Conference APMC2016, which is going to be held in India. He is a member of IEEE MTT-S Meetings and Symposia Committee (AdCom sub-committee).

Greg Bain is the Acting Research Leader Aircraft Performance and Survivability within the Aerospace Division. He has previously led research programs focused on the measurement, modelling and control of aircraft infrared signatures as well as aerospace composite technologies. More recently, he has led research into the sustainment of next generation microwave systems. Greg has previously held the Canberra based position of Air Force Scientific Adviser. He has a B.Sc (Hons.) in Mathematics, M.Eng. in Aeroacoustics and a PhD in Computational Fluid Dynamics from the University of Sydney.